Journal of Materials Chemistry C

PAPER

View Article Online
View Journal | View Issue





Cite this: J. Mater. Chem. C, 2019, 7, 3945

# Low-dimensional formamidinium lead perovskite architectures *via* controllable solvent intercalation†

Mingue Shin, ‡[a] Joonyun Kim, ‡[a] Young-Kwang Jung, ‡[b] Tero-petri Ruoko, [c] Arri Priimagi, [c] Aron Walsh *[bd] and Byungha Shin *[a]

Received 21st January 2019,
Accepted 7th March 2019

DOI: 10.1039/c9tc00379g

rsc.li/materials-c

We report the formation of a new class of solvent-intercalated two-dimensional (SI-2D) formamidinium lead halide perovskites. They can be mixed with three-dimensional (3D) stoichiometric perovskites by controlling the ratio of the precursor solutions. The composite leads to greatly improved photoluminescence quantum yield (PLQY) over the 3D compound. The enhanced PLQY is attributed to a type-I band alignment between the 3D and SI-2D, as revealed by first-principles calculations, which results in confined excitons with enhanced radiative recombination. The films exhibited excellent thermal and air stability retaining PLQY > 20% over 2 months in ambient conditions. Assemblies of halide perovskites with mixed dimensionality offer a pathway to enhance optoelectronic performance and device lifetimes.

## Introduction

Organic–inorganic halide perovskites have shown unparalleled progress in photovoltaics,[1–8] recently achieving power conversion efficiencies (PCEs) of 23.3%.[9] This is due to excellent optoelectronic properties of the perovskite, which include low concentrations of non-radiative defects,[10–12] high optical absorption coefficients with a sharp band edge[13,14] (*i.e.*, small Urbach tails) and photon recycling.[15] These properties also make the perovskite attractive for other optoelectronic applications such as light-emitting diodes (LEDs),[16–25] lasers[26] and gas sensors.[27]

The three dimensional (3D) perovskite has a structure of $AMX_3$, in which divalent metal cations, 'M', and halide anions, 'X', form a network of corner sharing $[MX_6]^{4-}$ octahedra. The monovalent cations, 'A', occupy sites surrounded by eight adjacent octahedra.[28] The incorporation of excess A′ cations can separate metal halide octahedra leading to the formation of the so-called low dimensional perovskite, which exhibits structural flexibility and optoelectronic properties vastly different from its 3D counterpart.[29–31] The typical candidates of A′ are long organic cations such as phenylmethylammonium[34] (PMA), phenylethylammonium[19,24] (PEA), butylammonium[22] (BA), 1-naphthylmethylamine[38] (NMA) and 2,2′-(ethylenedioxy)-bis(ethylammonium)[39] (EDBD). Especially, the 2D layered perovskites with the formula of $A'_2A_{m-1}M_mX_{3m+1}$[32] have drawn attention for LED applications[19,22,24,33–38] due to strong light emission originating from exciton and/or dielectric confinement effects.[39,40] Alternating layers of A′ cations and $[MX_6]$ octahedra form a natural multi-quantum-well structure in a molecular level. The 2D perovskite has been further shown to improve moisture stability[41] compared to the 3D perovskite arising from hydrophobic nature of long alkylammonium cation, thereby preventing the penetration of moistures into the lattices. Organic solvent such as benzene or hexane can be also intercalated between layers of the organic cations of the 2D perovskite, which has been shown to significantly alter optical and electrical properties.[42–44] Furthermore, studies have reported that precursor solutions with excess 'AX' organic halide affect colloidal status of the solutions and also extend the compositional phase field.[52,53]

In this work, we report formamidinium (FA) lead bromide perovskite thin films with mixed dimensionality—3D stoichiometric perovskite and a new class of two-dimensional perovskite intercalated with solvent molecules (SI-2D)—by controlling the $FABr/PbBr_2$ ratio in the precursor solutions. The new 2D phase consists of $FA_2PbBr_4$ intercalated with dimethyl sulfoxide (DMSO). In FABr-rich condition, excess formamidinium cations

[a] Department of Materials Science and Engineering, Korea Advanced Institute of Science and Technology (KAIST), Daejeon 34141, Republic of Korea. E-mail: byungha@kaist.ac.kr
[b] Department of Materials Science and Engineering, Yonsei University, Seoul 03722, Republic of Korea
[c] Laboratory of Chemistry and Bioengineering, Tampere University of Technology, P.O. Box 541, FI-33101, Tampere, Finland
[d] Department of Materials, Imperial College London, Exhibition Road, London SW7 2AZ, UK. E-mail: a.walsh@imperial.ac.uk

† Electronic supplementary information (ESI) available: Experimental methods, first principles calculation details, XRD, FT-IR, digital photos, optical characterization details (absorption spectra, steady-state PL spectra, TRPL, TRES and DAS) and schematic. See DOI: 10.1039/c9tc00379g

‡ These authors have contributed equally.

in the precursor solution interacts with DMSO molecules *via* hydrogen bonding creating $FA^+$–DMSO–$FA^+$ organic spacers and resulting in the separation of $[PbX_6]^{4-}$ networks along [001] direction. Density functional theory (DFT) calculations suggest a type-I band alignment between the 3D $FAPbBr_3$ with a smaller bandgap and the 2D $FA_2PbBr_4$–DMSO with a larger bandgap, which results in exciton confinement in the 3D phase and much improved PLQY (photoluminescence quantum yield). The films with the mixed dimensionality also exhibited excellent air and thermal stability.

## Results and discussion

Fig. 1a summarizes the fabrication of FA lead halide thin films. We varied the molar ratio of $FABr/PbBr_2$ (henceforth, referred to as $R$) of the precursor solution to 1, 1.2, 1.5 and 2 using DMSO as solvent. All films were spin-coated with anti-solvent (chlorobenzene) dripping and annealed at 80 °C for 10 minutes to crystallize and evaporate residual solvents. As shown in Fig. 1b and c, the color of the films turns from orange to pale yellow as $R$ increases and PL emission under UV light gradually becomes brighter. Especially, in the case of $R$ = 2, a noticeable blue shift of the PL emission is evident.

In order to investigate the cause of the changes in the optical properties with the varying $R$, further materials characterization was carried out. X-ray diffraction (XRD) patterns of the films confirm the formation of cubic crystal phase; (100) peak in XRD corresponds to a lattice parameter of 6.006 Å (space group $Pm\bar{3}m$), consistent with the known value for $FAPbBr_3$ (Fig. 2a). However, the diffraction pattern of $R$ = 2 shows additional peaks at $2\theta$ = 6.91° and 13.84°, suggesting the formation of a new crystal phase that coexists with $FAPbBr_3$. The film with $R$ = 1.5 also exhibits a peak, though weak, at $2\theta$ = 6.91°. The XRD peaks of this new crystal phase do not match to any known powder XRD patterns of FABr or $PbBr_2$ (Fig. S1, ESI†). Fig. 2b and c present absorbance and PL spectra, respectively. As the $R$ increases, the band edge excitonic absorption feature near 550 nm, corresponding to the known band gap of $FAPbBr_3$ (2.25 eV),[45] becomes gradually less pronounced and the PL intensity increases with gradual blue-shift of the emission. The film with $R$ = 2 exhibits emission at the wavelength of 531 nm with PLQY of 13.7%, which is much stronger than the emission from $R$ = 1 at 548 nm with PLQY of 0.4%; PLQYs of $R$ = 1.2 and 1.5 are 0.5% and 1.9%, respectively. One may speculate that the observed blue-shift is due to quantum-size effect. However, the FWHM of the (100) XRD peak remains nearly constant (Fig. S2, ESI†), which suggests that there is no significant change in the crystal size. Tauc plots (Fig. S3, ESI†) show an absorption edge near 3.1 eV for $R$ = 2, which must be originated from the new crystal phase identified from the XRD. Given the wider lattice spacing and a larger bandgap of the new crystal phase compared to the 3D $FAPbBr_3$, a strong candidate of the new phase is low-dimensional FA lead bromide. The emission wavelength of $R$ = 1 falls short of ~10 nm from the absorption edge indicating a small Stokes shift. Despite the apparent blue-shift of the emission wavelength with the increasing $R$, the emission from the $R$ = 2 films is still from the 3D phase part (*i.e.*, $FAPbBr_3$) of the film because the excitation wavelength (420 nm) was larger than the absorption edge at ~390 nm corresponding to the bandgap of the new phase. The PL blue shift and improved PLQY at $R$ = 2, therefore, are attributed to exciton or dielectric confinement effect, which is confirmed by the DFT calculation as discussed later.

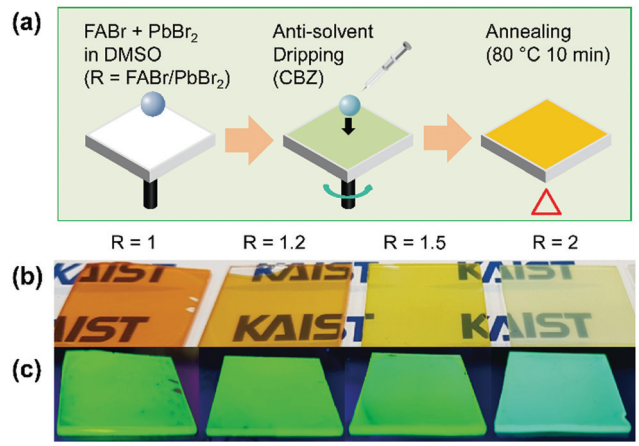


Fig. 1 Fabrication of formamidinium (FA) lead bromide thin films. (a) Schematic illustration of spin-coating with a variable molar ratio ($FABr/PbBr_2$ = R). (b and c) Digital photos of composition-controlled perovskite thin films ($R$ = 1, 1.2, 1.5 and 2) on a glass substrate without and with UV light (365 nm).

FT-IR spectra (Fig. 2d and Fig. S4, ESI†) reveal that with the increasing $R$, peaks originating from N–H stretch mode and C–H bend mode of the FA cations shift to smaller wavenumbers (from 3408 $cm^{-1}$, 3363 $cm^{-1}$, 3275 $cm^{-1}$, 3167 $cm^{-1}$ (N–H) and 1350 $cm^{-1}$ (C–H), when $R$ = 1 or 1.2, to 3388 $cm^{-1}$, 3350 $cm^{-1}$, 3237 $cm^{-1}$, 3162 $cm^{-1}$ (N–H) and 1331 $cm^{-1}$ (C–H), when $R$ = 1.5 and 2). This indicates that vibration of the FA cations is influenced by the new crystal phase. Interestingly, only in the case of the film with $R$ = 2 a new peak emerges at ~1400 $cm^{-1}$. This peak is attributed to the antisymmetric C–H bend mode of $CH_3$ ($\delta_{as}CH_3$) which cannot be from the FA molecules because it is absent in the films other than $R$ = 2 (and $R$ = 1.5 which shows a weak and broad bump); DMSO,[46] the solvent used for our solution process, must be responsible for the peak. Apparently, the formation of what we speculate to be a low-dimensional FA lead bromide seems to include DMSO when $R$ = 2 (and smaller amount when $R$ = 1.5). It is therefore concluded that DMSO molecules can be more readily trapped in the low-dimensional structure.

Since the new phase was formed under FABr excess conditions ($R$ = 2), it is likely to be a low-dimensional FABr-rich perovskite such as $FA_2PbBr_4$ (2D), $FA_3PbBr_5$ (1D) or $FA_4PbBr_6$ (0D). The unidentified XRD peak positions can give us a clue as to the origin of the new phase; however, there is no report of XRD patterns of the low dimensional FA lead bromide in literature. Therefore, we have simulated the crystal structure of these low-dimensional phases including optimization of the lattice shape, size and internal positions based on the stress tensors and atomic forces calculated from DFT. The corresponding diffraction peaks for the proposed structures are

 

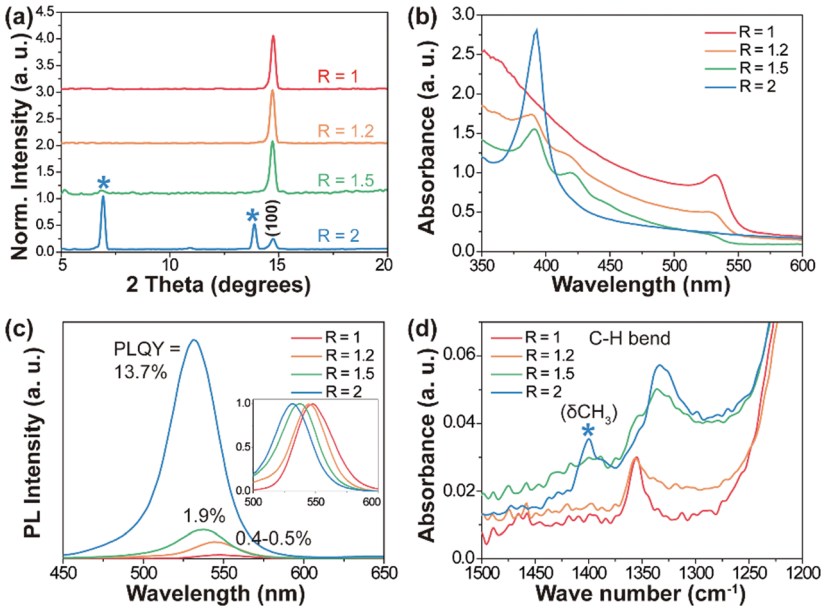


Fig. 2 Structural and optical characterization of FA lead bromide films with a varying precursor molar ratio, $R$ = 1, 1.2, 1.5 and 2. The films were spin-coated on a glass substrate and annealed at 80 °C for 10 minutes after the spin-coating. (a) Normalized XRD patterns, (b) absorbance, (c) steady-state PL at 420 nm of excitation wavelength, (inset: normalized spectra) and (d) magnified FT-IR absorbance spectra showing C–H bend.

shown in Fig. 3d. We considered models with and without intercalated DMSO solvent. (002) and (004) peaks of 2D $FA_2PbBr_4$–DMSO match the unidentified peaks from the $R$ = 2 suggesting that the new phase is 2D $FA_2PbBr_4$ intercalated with DMSO, consistent with the FT-IR results. The associated electronic band offsets shown in Fig. 3e confirms a type-I band alignment, which should lead to effective confinement of electrons and holes in the 3D perovskite.

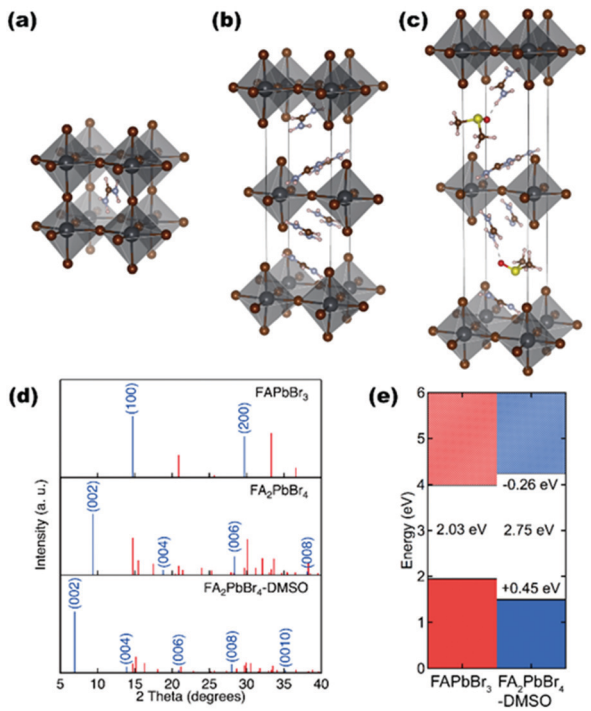


Fig. 3 Atomic crystal structure models of (a) $FAPbBr_3$, (b) $FA_2PbBr_4$ and (c) $FA_2PbBr_4$–DMSO. (d) Simulated XRD patterns of $FAPbBr_3$, $FA_2PbBr_4$ and $FA_2PbBr_4$–DMSO. (e) Calculated band alignment from HSE06 with HF 43% + SOC of $FAPbBr_3$ and $FA_2PbBr_4$–DMSO.

Knowing that there are residual DMSO intercalated into the 2D $FA_2PbBr_4$ in the $R$ = 2 films annealed at 80 °C, we increased the post-synthesis annealing temperature to examine the stability of the DMSO within the 2D $FA_2PbBr_4$ and luminescence. With the increasing annealing temperature up to 180 °C, the color of the films ($R$ = 2) becomes yellowish and PL emission becomes greenish (Fig. S5, ESI†). Fig. S6a (ESI†) shows XRD patterns of $R$ = 2 films with three different annealing conditions. In the non-annealed case (the solvent naturally dried in air after the spin-coating), only peaks from the low-dimensional $FA_2PbBr_4$–DMSO phase are observed. With thermal annealing, peaks from the 3D $FAPbBr_3$ emerge and their intensity increases with the annealing temperature while the peak intensity of the 2D $FA_2PbBr_4$–DMSO reduces. This indicates that thermal input transforms the 2D $FA_2PbBr_4$–DMSO into the 3D $FAPbBr_3$, which is presumably activated by de-intercalation of DMSO from the 2D structure. In addition, absorbance spectra (Fig. S6b, ESI†) show that the 120 °C-annealed film exhibit absorption edge near 530 nm, though weak, corresponding to the band gap of the 3D $FAPbBr_3$, consistent with the XRD pattern. The type-I band alignment (Fig. 3e) leads to efficient exciton confinement and higher luminescence. However, the relative amount of 3D to 2D, which can be controlled by the annealing temperature influences PLQY (see Fig. S6a and S7, ESI†). The highest PLQY of 35.7% was obtained from the 120 °C-annealed film and the higher annealing temperatures reduced PLQY.

We have confirmed the presence of the DMSO in the low-dimensional phase. Based on the XRD peak positions

(Fig. S6a, ESI†) and FT-IR (Fig. S8, ESI†) showing C–H bending of the DMSO at ~1400 $cm^{-1}$, the DMSO remains in the films annealed even at 120 °C although the amount of the total DMSO (and the 2D $FA_2PbBr_4$ hosting the DMSO) reduces with the annealing temperature as evident from the weaker XRD and FT-IR peaks. For comparison, FT-IR spectrum of the $R = 1$ film (*i.e.*, no 2D phase) annealed at 120 °C is included in Fig. S8 (ESI†). The spectrum reveals the absence of DMSO, suggesting that 120 °C is high enough to fully evaporate DMSO when forming 3D $FAPbBr_3$; only when DMSO is "trapped" in the 2D perovskite does it exhibit an extended thermal stability.

The thermal stability of DMSO within 2D $FA_2PbBr_4$ is further supported by thermodynamics calculation. We calculated the intercalation energy of DMSO in the low-dimensional phase following ($\Delta H^{intercal}_{DMSO}$) using

$$\Delta H^{intercal}_{DMSO} = E^{tot}_{FA_2PbBr_4-DMSO} - \left(E^{tot}_{FA_2PbBr_4} + E^{tot}_{DMSO}\right)$$

where $E^{tot}_{FA_2PbBr_4-DMSO}$, $E^{tot}_{FA_2PbBr_4}$, and $E^{tot}_{DMSO}$ are the (DFT) total energy of $FA_2PbBr_4$–DMSO, $FA_2PbBr_4$, and DMSO molecule, respectively. The calculated $\Delta H^{intercal}_{DMSO}$ is −0.23 eV per DMSO molecule, which indicates the intercalation of DMSO is a spontaneous (exothermic) reaction. To understand the nature of the interaction between $FA_2PbBr_4$ and DMSO, we plotted the charge density difference (Fig. S9, ESI†) and identified the formation of hydrogen bonding between DMSO and $FA^+$ molecular cation (SO···HN). This indicates that DMSO acts like a glue between adjacent $FA_2PbBr_4$ layers.

Interesting emission behavior was found from the films consisting of 3D $FAPbBr_3$ and 2D $FA_2PbBr_4$–DMSO. Fig. 4 shows excitation wavelength dependent steady-state PL spectra ($\lambda_{exc}$ = 320, 370, 420 and 470 nm) with different annealing conditions. To our surprise, the non-annealed film shows that emission wavelength linearly changes with the excitation wavelength; when the excitation wavelength is varied from 470 nm to 320 nm, the emission wavelength also blue-shifts by the same difference, ~50 nm. In the 80 °C-annealed film, the emission wavelength is still dependent on the excitation wavelength, however, the degree of the dependence becomes weaker than the non-annealed film. From the 120 °C-annealed film, no excitation wavelength dependence is observed. For comparison, we have also measured PL spectra from films with $R < 2$ annealed at 80 °C at various excitation wavelengths and the results are shown in Fig. S9 (ESI†) (PL spectra in Fig. S9d, ESI† are the same as Fig. 4b but they are still included in Fig. S9, ESI† for the purpose of comparison). We immediately see that when $R < 2$, steady-state PL is independent of the wavelength of the excitation source. $FAPbBr_3$ ($R = 1$) film without annealing is also excitation wavelength-independent (Fig. S10, ESI†). Combining the results of Fig. 4 and Fig. S9 (ESI†), we conclude that the necessary condition for the tunable emission wavelength by the excitation wavelength is the presence of the 2D $FA_2PbBr_4$–DMSO (*i.e.*, $R = 2$) more than a threshold amount (*i.e.*, annealing temperature ≤80 °C). Similar unusual emission characteristics have been reported from carbon nanodots and graphene oxide derivatives dispersed in polar solvents[47] or room temperature ionic liquids,[48] which was attributed to solvent relaxation effects.[49–51] A similar mechanism may operate in our case and the schematic of this mechanism is shown in Fig. S11 (ESI†).

To further understand the dynamics of charge recombination and PL emission, we have performed extensive time-resolved photoluminescence (TRPL) measurements at various monitoring wavelengths between 450 nm and 600 nm under two different excitation wavelengths of 375 nm and 483 nm (Fig. 5a–d). These wavelengths were chosen such that one wavelength (375 nm) is at a higher energy than the main absorption of the 2D phase (~390 nm from Fig. S6, ESI†) while the other wavelength (483 nm) is mainly absorbed by the tail states. For all monitoring wavelengths, TRPL decay curves were fitted with the same global fitting function with three exponential decays ($\tau_1$, $\tau_2$, $\tau_3$) using the following formula:

$$I(t) = \sum A_i e^{t/\tau_i} \quad (i = 1, 2, 3),$$

where $A_i$ ($i$ = 1, 2, 3) is a weighting factor of each decay component. A time-resolved emission spectrum (TRES) can be then constructed by plotting the intensities of the TRPL curves at a given time as a function of the monitoring wavelength (Fig. 5e–h). At the 375 nm excitation wavelength, the both films (80 °C- and 120 °C-annealed) exhibit an initial emission peak near 480 nm, which then gradually red-shifts over time. However, when the longer excitation wavelength of 483 nm is used

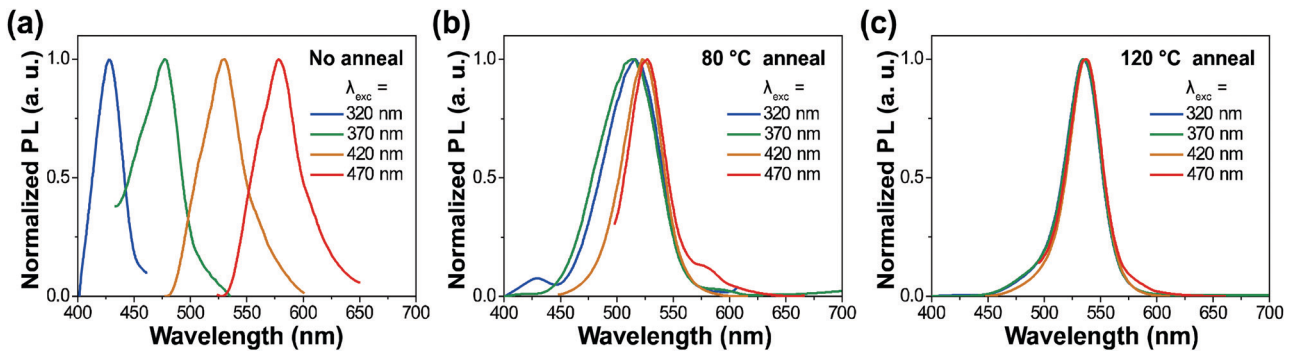


Fig. 4 Normalized steady-state PL spectra from films with $R = 2$ at different excitation wavelengths ($\lambda_{exc}$ = 320, 370, 420 and 470 nm). (a) No annealing (dried at room temperature), (b) annealed at 80 °C and (c) annealed at 120 °C.

 

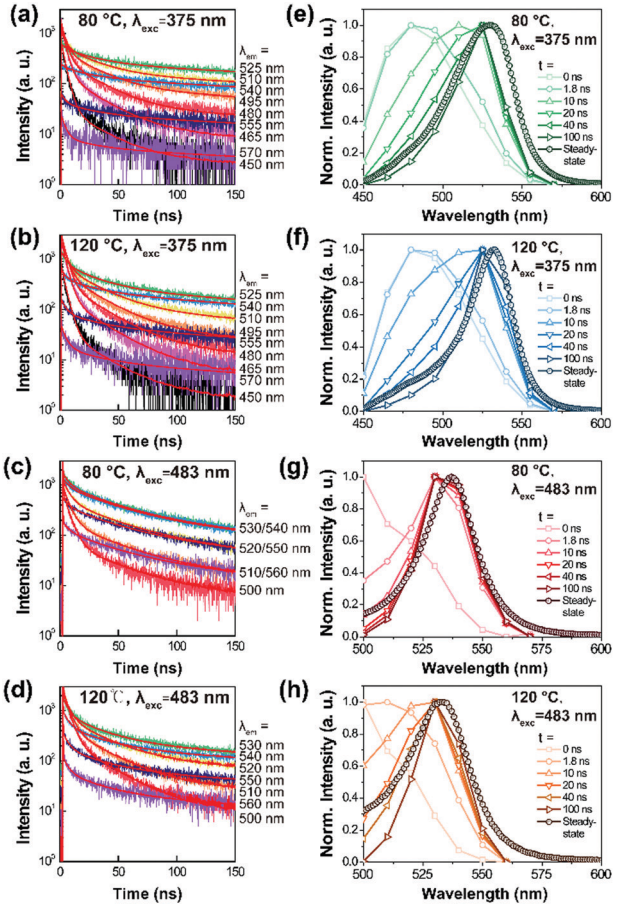


Fig. 5 (a–d) TRPL measurements at various monitoring wavelengths (450–600 nm) and (e–h) corresponding TRES data from the films with $R$ = 2 annealed at 80 °C and 120 °C. Two different excitation wavelengths were used (a, b, e, f for 375 nm and c, d, g, h for 483 nm).

(Fig. 5d and h), the initial red-shift of emission spectrum is faster in the 80 °C-annealed case than the 120 °C-annealed case (see also Fig. S13, ESI†). The 80 °C-annealed film exhibits more pronounced tail states in the absorption spectrum compared to the 120 °C-annealed film (Fig. S6, ESI†), presumably due to a higher concentration of the residual DMSO; therefore, it would suffer a larger degree of the solvent relaxation and is expected to show faster red-shift. To identify the emission spectra of each decay component, the weighting factors $A_i$, of the three decay components, $\tau_i$ are plotted as a function of wavelength (Fig. S14, ESI†), which is called decay associated spectrum (DAS). The DAS of the fastest decay component has an emission peak near 480 nm and is considered as the emission profile from the 2D $FA_2PbBr_4$–DMSO because the emission peak energy is larger than the measured band gap of the 3D $FAPbBr_3$. The slowest decay component, on the other hand, corresponds to the emission of the 3D $FAPbBr_3$. The middle decay component (green lines in Fig. S14, ESI†) could be mixed emission from the 2D $FA_2PbBr_4$–DMSO and the 3D $FAPbBr_3$, but its origin is not clear at the moment. Because there is no decay component with negative intensity in the DAS, no energy transfers from the 2D $FA_2PbBr_4$–DMSO to the 3D $FAPbBr_3$ is

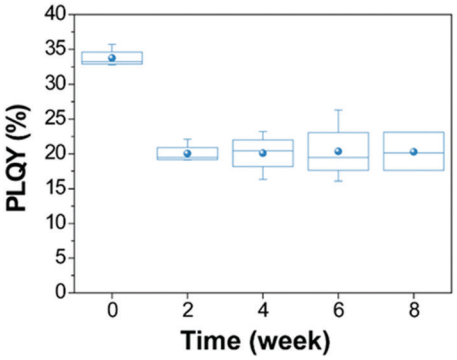


Fig. 6 PLQY of the 120 °C-annealed $R$ = 2 composite films stored in air over 8 weeks.

inferred; otherwise, a temporary enhancement of PL intensity (*i.e.*, negative decay) should be observed. On the contrary, TRPL spectra from the $R$ = 1 film at various monitoring wavelengths exhibit a single component exponential decay with a relatively long lifetime of 150 ns and thus it shows emission profiles that is independent on excitation wavelength (Fig. S15, ESI†).

We also examined the thermal and air stability of the $R$ = 2 films including the one with the highest PLQY (35.7%), *i.e.*, $R$ = 2, annealed at 120 °C. Fig. S5 (ESI†) shows the photos and PL emission under UV light of $R$ = 1 and $R$ = 2 films with different annealing temperatures. In the $R$ = 1 films, PL intensity rapidly decreased when annealed at 120 °C. On the other hand, the $R$ = 2 films emit bright PL even when annealed at 180 °C even though the PLQY value reduced to ~5%. Furthermore, the highest PLQY film maintained PLQY over 20% even after 2 months of storage in the ambient condition (Fig. 6), indicating an excellent air stability.

Furthermore, we have replaced the solvent with dimethylformamide (DMF) to test the intercalation of solvent molecules other than DMSO to the 2D perovskite. We also found XRD peak at $2\theta = 6.9°$ as is the case when DMSO was used as the solvent (Fig. S16, ESI†). This suggests that 2D perovskite intercalated with DMF still forms. Note that DMF has a similar molecular size and dimethyl group as DMSO. However, unlike the DMSO case, the relative portion of the 2D perovskite, as examined by XRD, is smaller and 3D perovskite dominated even without annealing. Annealing at a high enough temperature such as 120 °C made the 2D disappear by the de-intercalation of DMF (see Fig. S16, ESI†). PL spectra of the non-annealed film has a weak excitation wavelength dependence. This dependence disappeared when annealed at 80 °C (see Fig. S17, ESI†) possibly because the content of solvent molecules present in the 2D perovskite is not enough to cause the excitation wavelength dependent PL when DMF is used as the solvent. This is understandable because DMF has a higher vapor pressure. Hence, solvent intercalation is more controllable when DMSO is used.

## Conclusions

By controlling the $FABr/PbBr_2$ ratio in the precursor solutions, films with mixed dimensionality were formed. A combination

of materials characterization (XRD, FT-IR) and first-principles simulations indicates that the films consist of 3D $FAPbBr_3$ and 2D $FA_2PbBr_4$ intercalated with DMSO, a solvent used in the precursor solution. The 2D $FA_2PbBr_4$–DMSO exhibited unusual optical properties—tunable PL emission wavelength that is dependent on the wavelength of excitation source—due to the solvent relaxation process of DMSO molecules present in the 2D perovskite. A type-I band alignment between the 3D and 2D phases lead to efficient exciton confinement and therefore higher luminescence. The film retained PLQY more than 20% even after 8 weeks of storage in the air. This study points to the importance of forming halide perovskite films with the mixed dimensionality in order to maximize their potential for light emission. We have also shown the remarkably high thermal stability of DMSO, one of the typical solvents for the halide perovskite, when it is incorporated into the 2D perovskite phase.

## Conflicts of interest

There are no conflicts to declare.

## Acknowledgements

The work at KAIST was supported by Nano Material Technology Development Program (Green Nano Technology Development Program) through the National Research Foundation of Korea (NRF) funded by the Ministry of Education, Science and Technology (No. 2018M3A7B4065662) and National Research Foundation of Korea (NRF) grant funded by the Korea government (No. NRF-2018R1A5A1025594). The work at Yonsei was supported by the Creative Materials Discovery Program through the National Research Foundation of Korea (NRF) funded by Ministry of Science and ICT (2018M3D1A1058536). The work at ICL was supported by the Royal Society and the Leverhulme Trust. *Via* our membership of the UK's HEC Materials Chemistry Consortium, which is funded by EPSRC (EP/L000202), this work used the ARCHER supercomputing service. The work at TUT was funded by the Academy of Finland (Grant Number 311142), and by the TUT-KAIST seed funding provided by TUT.

## References

1 N. J. Jeon, J. H. Noh, Y. C. Kim, W. S. Yang, S. Ryu and S. I. Seok, *Nat. Mater.*, 2014, **13**, 897–903.
2 A. Kojima, K. Teshima, Y. Shirai and T. Miyasaka, *J. Am. Chem. Soc.*, 2009, **131**, 6050–6051.
3 M. M. Lee, J. Teuscher, T. Miyasaka, T. N. Murakami and H. J. Snaith, *Science*, 2012, **338**, 1228604.
4 D.-Y. Son, J.-W. Lee, Y. J. Choi, I.-H. Jang, S. Lee, P. J. Yoo, H. Shin, N. Ahn, M. Choi, D. Kim and N.-G. Park, *Nat. Energy*, 2016, **1**, 16081.
5 A. Abate, M. Saliba, D. J. Hollman, S. D. Stranks, K. Wojciechowski, R. Avolio, G. Grancini, A. Petrozza and H. J. Snaith, *Nano Lett.*, 2014, **14**, 3247.
6 W. S. Yang, B.-W. Park, E. H. Jung, N. J. Jeon, Y. C. Kim, D. U. Lee, S. S. Shin, J. Seo, E. K. Kim and J. H. Noh, *Science*, 2017, **356**, 1376–1379.
7 D. Kim, G. Y. Kim, C. Ko, S. R. Pae, Y. S. Lee, O. Gunawan, D. F. Ogletree, W. Jo and B. Shin, *J. Phys. Chem. C*, 2016, **120**, 21330–21335.
8 S. R. Pae, S. Byun, J. Kim, M. Kim, I. Gereige and B. Shin, *ACS Appl. Mater. Interfaces*, 2018, **10**, 534–540.
9 NREL Solar Cell Efficiency Chart, https://www.nrel.gov/pv/assets/pdfs/pv-efficiencies-07-17-2018.pdf, accessed November 09, 2018.
10 J. Kim, S. H. Lee, J. H. Lee and K. H. Hong, *J. Phys. Chem. Lett.*, 2014, **5**, 1312–1317.
11 W. J. Yin, T. Shi and Y. Yan, *Adv. Mater.*, 2014, **26**, 4653–4658.
12 W.-J. Yin, T. Shi and Y. Yan, *Appl. Phys. Lett.*, 2014, **104**, 063903.
13 S. De Wolf, J. Holovsky, S. J. Moon, P. Loper, B. Niesen, M. Ledinsky, F. J. Haug, J. H. Yum and C. Ballif, *J. Phys. Chem. Lett.*, 2014, **5**, 1035–1039.
14 A. Sadhanala, F. Deschler, T. H. Thomas, S. E. Dutton, K. C. Goedel, F. C. Hanusch, M. L. Lai, U. Steiner, T. Bein, P. Docampo, D. Cahen and R. H. Friend, *J. Phys. Chem. Lett.*, 2014, **5**, 2501–2505.
15 L. M. Pazos-Outón, M. Szumilo, R. Lamboll, J. M. Richter, M. Crespo-Quesada, M. Abdi-Jalebi, H. J. Beeson, M. Vrućinić, M. Alsari and H. J. Snaith, *Science*, 2016, **351**, 1430–1433.
16 H. Cho, S.-H. Jeong, M.-H. Park, Y.-H. Kim, C. Wolf, C.-L. Lee, J. H. Heo, A. Sadhanala, N. Myoung and S. Yoo, *Science*, 2015, **350**, 1222–1225.
17 J. W. Lee, Y. J. Choi, J. M. Yang, S. Ham, S. K. Jeon, J. Y. Lee, Y. H. Song, E. K. Ji, D. H. Yoon, S. Seo, H. Shin, G. S. Han, H. S. Jung, D. Kim and N. G. Park, *ACS Nano*, 2017, **11**, 3311–3319.
18 J. Li, L. Xu, T. Wang, J. Song, J. Chen, J. Xue, Y. Dong, B. Cai, Q. Shan, B. Han and H. Zeng, *Adv. Mater.*, 2017, **29**, 1603885.
19 L. N. Quan, Y. Zhao, F. P. Garcia de Arquer, R. Sabatini, G. Walters, O. Voznyy, R. Comin, Y. Li, J. Z. Fan, H. Tan, J. Pan, M. Yuan, O. M. Bakr, Z. Lu, D. H. Kim and E. H. Sargent, *Nano Lett.*, 2017, **17**, 3701–3709.
20 J. Si, Y. Liu, Z. He, H. Du, K. Du, D. Chen, J. Li, M. Xu, H. Tian, H. He, D. Di, C. Lin, Y. Cheng, J. Wang and Y. Jin, *ACS Nano*, 2017, **11**, 11100–11107.
21 Z. K. Tan, R. S. Moghaddam, M. L. Lai, P. Docampo, R. Higler, F. Deschler, M. Price, A. Sadhanala, L. M. Pazos, D. Credgington, F. Hanusch, T. Bein, H. J. Snaith and R. H. Friend, *Nat. Nanotechnol.*, 2014, **9**, 687–692.
22 Z. Xiao, R. A. Kerner, L. Zhao, N. L. Tran, K. M. Lee, T.-W. Koh, G. D. Scholes and B. P. Rand, *Nat. Photonics*, 2017, **11**, 108–115.
23 E. Yassitepe, Z. Yang, O. Voznyy, Y. Kim, G. Walters, J. A. Castañeda, P. Kanjanaboos, M. Yuan, X. Gong, F. Fan, J. Pan, S. Hoogland, R. Comin, O. M. Bakr, L. A. Padilha, A. F. Nogueira and E. H. Sargent, *Adv. Funct. Mater.*, 2016, **26**, 8757–8763.

 

24 M. Yuan, L. N. Quan, R. Comin, G. Walters, R. Sabatini, O. Voznyy, S. Hoogland, Y. Zhao, E. M. Beauregard, P. Kanjanaboos, Z. Lu, D. H. Kim and E. H. Sargent, *Nat. Nanotechnol.*, 2016, **11**, 872–877.
25 R. L. Hoye, M. R. Chua, K. P. Musselman, G. Li, M. L. Lai, Z. K. Tan, N. C. Greenham, J. L. MacManus-Driscoll, R. H. Friend and D. Credgington, *Adv. Mater.*, 2015, **27**, 1414–1419.
26 G. Xing, N. Mathews, S. S. Lim, N. Yantara, X. Liu, D. Sabba, M. Gratzel, S. Mhaisalkar and T. C. Sum, *Nat. Mater.*, 2014, **13**, 476–480.
27 H.-H. Fang, S. Adjokatse, H. Wei, J. Yang, G. R. Blake, J. Huang, J. Even and M. A. Loi, *Sci. Adv.*, 2016, **2**, e1600534.
28 D. B. Mitzi, *J. Chem. Soc., Dalton Trans.*, 2001, **1**, 1–12.
29 H. Lin, C. Zhou, Y. Tian, T. Siegrist and B. Ma, *ACS Energy Lett.*, 2017, **3**, 54–62.
30 M. I. Saidaminov, O. F. Mohammed and O. M. Bakr, *ACS Energy Lett.*, 2017, **2**, 889–896.
31 C. C. Stoumpos, L. Mao, C. D. Malliakas and M. G. Kanatzidis, *Inorg. Chem.*, 2017, **56**, 56–73.
32 Z. Cheng and J. Lin, *CrystEngComm*, 2010, **12**, 2646.
33 J. Byun, H. Cho, C. Wolf, M. Jang, A. Sadhanala, R. H. Friend, H. Yang and T. W. Lee, *Adv. Mater.*, 2016, **28**, 7515–7520.
34 M. Era, S. Morimoto, T. Tsutsui and S. Saito, *Appl. Phys. Lett.*, 1994, **65**, 676–678.
35 H. Hu, T. Salim, B. Chen and Y. M. Lam, *Sci. Rep.*, 2016, **6**, 33546.
36 R. Li, C. Yi, R. Ge, W. Zou, L. Cheng, N. Wang, J. Wang and W. Huang, *Appl. Phys. Lett.*, 2016, **109**, 151101.
37 N. Wang, L. Cheng, R. Ge, S. Zhang, Y. Miao, W. Zou, C. Yi, Y. Sun, Y. Cao, R. Yang, Y. Wei, Q. Guo, Y. Ke, M. Yu, Y. Jin, Y. Liu, Q. Ding, D. Di, L. Yang, G. Xing, H. Tian, C. Jin, F. Gao, R. H. Friend, J. Wang and W. Huang, *Nat. Photonics*, 2016, **10**, 699–704.
38 S. Zhang, C. Yi, N. Wang, Y. Sun, W. Zou, Y. Wei, Y. Cao, Y. Miao, R. Li, Y. Yin, N. Zhao, J. Wang and W. Huang, *Adv. Mater.*, 2017, **29**, 1606600.
39 E. R. Dohner, A. Jaffe, L. R. Bradshaw and H. I. Karunadasa, *J. Am. Chem. Soc.*, 2014, **136**, 13154–13157.
40 Z. Yuan, Y. Shu, Y. Xin and B. Ma, *Chem. Commun.*, 2016, **52**, 3887–3890.
41 S. Yang, Y. Wang, P. Liu, Y.-B. Cheng, H. J. Zhao and H. G. Yang, *Nat. Energy*, 2016, **1**, 15016.
42 Y. I. Dolzhenko, T. Inabe and Y. Maruyama, *Bull. Chem. Soc. Jpn.*, 1986, **59**, 563–567.
43 K. Liang, D. B. Mitzi and M. T. Prikas, *Chem. Mater.*, 1998, **10**, 403–411.
44 D. B. Mitzi, D. R. Medeiros and P. R. Malenfant, *Inorg. Chem.*, 2002, **41**, 2134–2145.
45 L. Protesescu, S. Yakunin, M. I. Bodnarchuk, F. Bertolotti, N. Masciocchi, A. Guagliardi and M. V. Kovalenko, *J. Am. Chem. Soc.*, 2016, **138**, 14202–14205.
46 V. M. Wallace, N. R. Dhumal, F. M. Zehentbauer, H. J. Kim and J. Kiefer, *J. Phys. Chem. B*, 2015, **119**, 14780–14789.
47 Z. Gan, H. Xu and Y. Hao, *Nanoscale*, 2016, **8**, 7794–7807.
48 A. Samanta, *J. Phys. Chem. B*, 2006, **110**, 13704–13716.
49 S. K. Cushing, M. Li, F. Huang and N. Wu, *ACS Nano*, 2013, **8**, 1002–1013.
50 S. Khan, A. Gupta, N. C. Verma and C. K. Nandi, *Nano Lett.*, 2015, **15**, 8300–8305.
51 A. Sharma, T. Gadly, A. Gupta, A. Ballal, S. K. Ghosh and M. Kumbhakar, *J. Phys. Chem. Lett.*, 2016, **7**, 3695–3702.
52 Z. Song, S. C. Watthage, A. B. Phillips, B. L. Tompkins, R. J. Ellingson and M. J. Heben, *Chem. Mater.*, 2015, **27**, 4612–4619.
53 K. Yan, M. Long, T. Zhang, Z. Wei, H. Chen, S. Yang and J. Xu, *J. Am. Chem. Soc.*, 2015, **137**, 4460–4468.